

Numerical Simulation for Moving Contact Line with Continuous Finite Element Schemes

Yongyue Jiang^{1,*}, Ping Lin², Zhenlin Guo³ and Shuangling Dong⁴

¹ School of Mathematics and Physics, University of Science and Technology, Beijing 100083, P.R. China.

² Department of Mathematics, University of Dundee, Dundee DD1 4HN, Scotland, United Kingdom.

³ Department of mathematics, University of California Irvine, CA 92697-3875, 540H Rowland Hall, Irvine, USA.

⁴ School of Aerospace Engineering, Tsinghua University, Beijing 100084, P.R. China.

Communicated by Ming-Chih Lai

Received 17 March 2014; Accepted (in revised version) 16 January 2015

Abstract. In this paper, we compute a phase field (diffuse interface) model of Cahn-Hilliard type for moving contact line problems governing the motion of isothermal multiphase incompressible fluids. The generalized Navier boundary condition proposed by Qian et al. [1] is adopted here. We discretize model equations using a continuous finite element method in space and a modified midpoint scheme in time. We apply a penalty formulation to the continuity equation which may increase the stability in the pressure variable. Two kinds of immiscible fluids in a pipe and droplet displacement with a moving contact line under the effect of pressure driven shear flow are studied using a relatively coarse grid. We also derive the discrete energy law for the droplet displacement case, which is slightly different due to the boundary conditions. The accuracy and stability of the scheme are validated by examples, results and estimate order.

AMS subject classifications: 65M60, 76T10

Key words: Two-phase flow, generalized Navier boundary condition, continuous finite elements, moving contact line.

1 Introduction

Multiphase flows are common in our lives, for example, gas bubbles trapped and droplet of oil moved in water, biological fluids, and cells in blood, etc.. They play an important

*Corresponding author. *Email addresses:* jiangyongyue1987@sina.com (Y. Jiang), plin@maths.dundee.ac.uk (P. Lin)

role in engineering, biological and applications. For example, the inclusion removal of melted materials is carried out with the help of bubble flotation [2]. When a bubble rises to the edge of a container the interface changes its geometric property. This forms moving contact line problem. Moving contact line, where the fluid-fluid interface intersects the solid wall has been extensively studied by researchers both theoretically and experimentally. Norman and Miksis [3] investigated the dynamics of a gas bubble with a moving contact line rising in an inclined channel. Luo et al. [4] carried out a numerical simulation on the Poiseuille flow of two immiscible fluids between two parallel plates with undulating solid surface and showed the effect of the surface roughness on the motion of two phase flow. The formation of bubbles on an orifice plate was studied by Chen et al. [5]. In their works, two models are considered where one is a stick-slip model and the other one assumes that the apparent contact angle is linearly related to the velocity. Fuentes and Cerro [6] presented a model for two immiscible fluids, considering force balance and inertia effect. Nikolayev et al. [7] proposed a model that took into account of heterogeneities of the solid surface and the inertia effect. Zahedi et al. [8] applied the idea of driving contact line movement by enforcing the equilibrium contact angle at the boundary to that in the traditional model and solved the new model by a conservative level set method. Gerbeau and Lelivre [9] numerically simulated two immiscible fluids between two parallel walls and performed a stability analysis in the energy norm with the consideration of the gravity and surface tension effects. Xu and Wang [10] analyzed the effect of the roughness of the rough surface on moving contact line. Jacqmin [11] investigated moving contact line dynamics of CHW (Cahn-Hilliard-van der Waals) diffuse mean-field interface. The convection or the diffusion driven by chemical potential gradients would cause the change of the interface. This phase field model was compared with the classical sharp interface model.

The change of the contact line as the fluid flows is of great interest where the boundary condition of a moving contact line is crucial. A no-slip condition holds on the boundary may lead to a force singularity in the vicinity of the contact line. This is why moving contact line problems are more complicated than normal multiphase flow problems. Several works have been carried out to eliminate the singularity. The most popular viewpoint is to relax the no-slip condition by introducing a new parameter called slip length [12]. With this viewpoint, Qian et al. [1] proposed the generalized Navier boundary condition (GNBC) based on the molecular dynamics theory. With the help of GNBC that can be derived variationally from the principle of minimum energy dissipation [21], they successfully simulated the moving contact line in two chemically patterned channels. Several numerical methods have been developed for moving contact line problem, for example, immersed interface method [13], finite element method [14,25], the volume of fluid method [15], a hybrid atomistic-continuum method [16] and moving mesh spectral method [17], etc. have been applied to moving contact line problems over the years. In addition, to construct a stable scheme, the energy of the system was made decreasing with time under certain conditions [19].

Among the models of multiphase flow problems, the phase field model attracts more and more attention recently. In a phase field model (or diffuse interface model, see [11]), the interface is considered to have a thickness and the change of flow-parameters from one phase to the other is continuous. Unlike sharp interface models, the two fluids in a phase field model are treated as one fluid and are mixed smoothly near the interfacial region, where the flow parameters change rapidly. This two fluid mixture may also be considered as a special kind of non-Newtonian fluids.

There is usually a physical energy law associated with the phase field model (see [21] for example). The preservation of the energy law turns out to be very important in designing a numerical method for such models. When a rapid change or a singularity occurs in the solution the preservation of energy law is more likely to produce correct evolution of the solution [20,22–24], even though a relatively coarse mesh is used. Therefore an energy law preserving method may reduce the cost of computational as well.

In this paper we propose an energy law preserving continuous finite element scheme to moving contact line problems based on the Cahn-Hilliard phase field model. The scheme in this paper is different from those in [14, 25]. In [14], the operator-splitting is used on the time-discretization. In [25], a convex splitting scheme is used for the Cahn-Hilliard equations, where an extra stabilization term is introduced to ensure the energetic stability of the scheme. In the spatial discretization, P_2 - P_0 mixed finite element method is directly applied to the Navier-Stokes equations with the inf-sup condition being satisfied.

The penalty method is introduced, which reformulates the continuous equation from index-2 problem to an index-1 problem so that the reformulated problem is more stable and more flexible in designing a temporal discretization [30–33]. We then design a modified midpoint temporal scheme where a discrete energy law that is approximately the same as the continuous energy law can be derived. The energetic stability is simply a by-product of the energy law.

This paper is organized as the following. In Section 2, we introduce the model, boundary conditions as well as its weak formulation and energy law. In Section 3, we present a fully discretized NSCH system with a continuous finite element method and a second order temporal scheme. The discrete energy law is also derived in Section 3. In Section 4, two kinds of immiscible fluids in a pipe and droplet displacement under the effect of pressure driven shear flow are simulated using our scheme which demonstrates that our scheme for moving contact line problems is stable and can produce correct solution of the evolution. The preservation of continuous energy law is also demonstrated. We will show that the total free energy increases by time during the simulation, whereas the sum of total free energy and the work done to the wall decreases by time. Our computations are carried out in a relatively coarse mesh to demonstrate that the robustness and efficiency of our energy law preserving scheme.

2 Phase field model, weak form and energy law

Let Ω be a bounded domain in \mathbb{R}^2 and Γ be the boundary of Ω (Lipschitz-continuous). Moving contact line problems can be modeled with a system which combines Cahn-Hilliard and Navier-Stokes equations with the generalized Navier boundary condition [1, 19, 25]

$$\frac{\partial \phi}{\partial t} + \mathbf{u} \cdot \nabla \phi = M \Delta \mu, \quad \mu = -K \Delta \phi - r \phi + \lambda \phi^3 \text{ (the chemical potential)}, \quad (2.1)$$

$$\nabla \cdot \mathbf{u} = 0, \quad (2.2)$$

$$\rho \left[\frac{\partial \mathbf{u}}{\partial t} + (\mathbf{u} \cdot \nabla) \mathbf{u} \right] = -\nabla p + \nabla \cdot \boldsymbol{\sigma} + \mu \nabla \phi, \quad \text{for all } \mathbf{x} = (x, z) \in \Omega. \quad (2.3)$$

Here $\mathbf{u} = (u_x, u_z)$ the velocity of the fluid mixture, where u_x denotes the velocity in the x direction and u_z the velocity in the z direction, p is the hydrostatic pressure, ϕ is the "phase" of the mixture ($\phi = 1$: fluid A; $\phi = -1$: fluid B), $\boldsymbol{\sigma} = \eta(\nabla \mathbf{u} + \nabla \mathbf{u}^T)$ denotes the viscous part of stress tensor, ρ and η the fluid density and viscosity coefficient which are assumed to be constants in this paper, M the phenomenological mobility coefficient and $\mu \nabla \phi$ the capillary force. As moving contact line problems we study occur in a pipe $\Omega = [-L_x/2, L_x/2] \times [-L_z/2, L_z/2]$, we define, as in [19], $\Gamma = \Gamma_T + \Gamma_B + \Gamma_L + \Gamma_R$ reflecting top(T), bottom(B), left(L), right(R) four edges. At first let's consider the moving contact line intersects boundaries T and B. The boundary conditions of Γ_T and Γ_B are

$$\beta u_x^{slip} = -\eta \partial_n u_x + L(\phi) \partial_x \phi, \quad (2.4)$$

$$\frac{\partial \phi}{\partial t} + u_x \partial_x \phi = -H[L(\phi)], \quad (2.5)$$

$$u_z = 0, \quad \partial_n \mu = 0, \quad (2.6)$$

where β is the slip coefficient. (n, τ) is normal and tangential directions to the boundary. H is a positive parameter, and the boundary conditions of Γ_L and Γ_R are

$$\partial_x \mathbf{u} = 0, \quad \partial_x \phi = 0, \quad \partial_x \mu = 0, \quad (2.7)$$

$$p(x, z) = \text{const}, \quad \partial_x p(x, z) = 0, \quad (2.8)$$

$$u_x(x, z) = -u_x(x, -z), \quad u_z(x, z) = 0. \quad (2.9)$$

In addition $L(\phi) = K \partial_n \phi + \partial \gamma_{wf}(\phi) / \partial \phi$ and $\gamma_{wf}(\phi) = -(1/2) \gamma \cos \theta_s^{surf} \sin(\frac{\pi}{2} \phi)$. K, r, λ are the parameters that are related to the interface thickness $\zeta = \sqrt{K/r}$, the interfacial tension $\gamma = 2\sqrt{2} r^2 \zeta / 3\lambda$ and also the phase variable $\phi = \sqrt{r/\lambda}$. θ_s^{surf} is the static contact angle. The dimensionless physical quantities are

$$\mathbf{U} = \frac{\mathbf{u}}{V}, \quad T = \frac{tV}{L}, \quad \varphi = \frac{\phi}{\sqrt{r/\lambda}}, \quad p^* = \frac{pL}{\eta V}, \quad \mathbf{X} = \frac{\mathbf{x}}{L}, \quad \epsilon = \frac{\sqrt{K/r}}{L}, \quad (2.10)$$

where L is the characteristic length of the fluids domain and V is the characteristic speed. Applying (2.10) to the system and without loss of generality letting $\mathbf{u} = \mathbf{U}$, $\mathbf{x} = \mathbf{X}$, $\phi = \varphi$, $t = T$, $p = p^*$, the system of NSCH becomes

$$\frac{\partial \phi}{\partial t} + \mathbf{u} \cdot \nabla \phi = L_d \Delta \mu^*, \quad \mu^* = -\epsilon \Delta \phi - \frac{1}{\epsilon} \phi + \frac{1}{\epsilon} \phi^3, \quad (2.11)$$

$$\nabla \cdot \mathbf{u} = 0, \quad (2.12)$$

$$Re \left[\frac{\partial \mathbf{u}}{\partial t} + (\mathbf{u} \cdot \nabla) \mathbf{u} \right] = -\nabla p + \Delta \mathbf{u} + B \mu^* \nabla \phi. \quad (2.13)$$

The boundary conditions of Γ_T and Γ_B become

$$\frac{1}{L_s} u_x^{slip} = -\partial_n u_x + B L_c(\phi) \partial_x \phi, \quad (2.14)$$

$$\frac{\partial \phi}{\partial t} + u_x \partial_x \phi = -V_s [L_c(\phi)], \quad (2.15)$$

$$u_z = 0, \quad \partial_n \mu^* = 0, \quad (2.16)$$

and the boundary conditions of Γ_L and Γ_R become

$$\partial_x u = 0, \quad \partial_x \phi = 0, \quad \partial_x \mu^* = 0, \quad (2.17)$$

$$p(x, z) = const, \quad \partial_x p(x, z) = 0, \quad (2.18)$$

$$u_x(x, z) = -u_x(x, -z), \quad u_z(x, z) = 0. \quad (2.19)$$

Here

$$Re = \frac{\rho V L}{\eta}, \quad B = \frac{\sqrt{K} r}{\eta V}, \quad L_d = \frac{M \sqrt{K} r}{L^2 V},$$

$$L_s = \frac{\eta}{\beta L}, \quad V_s = \frac{L H \sqrt{K} r}{V},$$

$$L_c(\phi) = \epsilon \partial_n \phi + \frac{\partial \gamma_{wf}^*(\phi)}{\partial \phi},$$

$$\gamma_{wf}^*(\phi) = -\frac{\sqrt{2}}{3} \cos \theta_s^{surf} \sin\left(\frac{\pi}{2} \phi\right).$$

We rewrite the phase field equations as

$$\frac{\partial \phi}{\partial t} + \mathbf{u} \cdot \nabla \phi = L_d \Delta (\omega + c\phi), \quad (2.20)$$

$$\omega + c\phi = \mu^* = -\epsilon \Delta \phi - \frac{1}{\epsilon} \phi + \frac{1}{\epsilon} \phi^3, \quad (2.21)$$

where the positive constant c is introduced to enhance the stability of the numerical method [20, 28]. As in [20], we deal with the divergence-free condition (2.12) by the penalty formulation

$$\nabla \cdot \mathbf{u} + \delta p = 0,$$

where δ is small penalty. The benefit of the penalty method is (i) an energy law may be derived relatively easily; (ii) an artificial boundary condition for the pressure p may be avoided.

Denote $\mathbf{W}^{1,3}(\Omega) = (W^{1,3}(\Omega))^2$, $\mathbf{L}^2(\Omega) = (L^2(\Omega))^2$ and $L_0^2(\Omega) = \{p \in L^2(\Omega), \int_{\Omega} p dx = 0\}$ as usual. Applying the idea in [20] to the present work, the weak form of the penalized NSCH system reads: Find $\mathbf{u} \in \mathbf{W}^{1,3}(\Omega)$, $p \in L_0^2(\Omega)$, $\phi \in (W^{1,3}(\Omega))$ and $\omega \in (W^{1,3}(\Omega))$ such that

$$\int_{\Omega} \left(\frac{\partial \phi}{\partial t} \psi + (\mathbf{u} \cdot \nabla \phi) \psi + L_d \nabla(\omega + c\phi) \cdot \nabla \psi \right) dx = 0, \quad \forall \psi \in W^{1,3}(\Omega), \tag{2.22}$$

$$\int_{\Omega} \left((\omega + c\phi) \chi - \epsilon \nabla \phi \cdot \nabla \chi - \frac{1}{\epsilon} (\phi^3 - \phi) \chi \right) dx + \int_{\Gamma_T, \Gamma_B} \left(L_c(\phi) \chi - \frac{\partial \gamma_{wf}^*(\phi)}{\partial \phi} \chi \right) ds = 0, \quad \forall \chi \in W^{1,3}(\Omega), \tag{2.23}$$

$$\int_{\Omega} (\nabla \cdot \mathbf{u} + \delta p) q dx = 0, \quad \forall q \in L_0^2(\Omega), \tag{2.24}$$

$$\int_{\Omega} \left(Re \left(\frac{\partial \mathbf{u}}{\partial t} \cdot \mathbf{v} + (\mathbf{u} \cdot \nabla) \mathbf{u} \cdot \mathbf{v} \right) - p(\nabla \cdot \mathbf{v}) + \nabla \mathbf{u} : \nabla \mathbf{v} - B(\omega + c\phi) \nabla \phi \cdot \mathbf{v} \right) dx + \int_{\Gamma_T, \Gamma_B} \left(\frac{1}{L_s} u_x^{slip} v_x - BL_c(\phi) \partial_x \phi v_x \right) ds = 0, \quad \forall \mathbf{v} \in \mathbf{W}^{1,3}(\Omega). \tag{2.25}$$

Letting $\psi = B(\omega + c\phi)$, $\mathbf{v} = \mathbf{u}$, $q = p$ and $\chi = B\partial\phi/\partial t$, the weak form becomes

$$\int_{\Omega} \left(B \frac{\partial \phi}{\partial t} (\omega + c\phi) + (B(\mathbf{u} \cdot \nabla \phi) (\omega + c\phi)) + BL_d |\nabla(\omega + c\phi)|^2 \right) dx = 0, \tag{2.26}$$

$$\int_{\Omega} \left(B(\omega + c\phi) \frac{\partial \phi}{\partial t} - B \frac{\partial}{\partial t} \left(\frac{\epsilon}{2} (\nabla \phi)^2 + \frac{1}{4\epsilon} (\phi^2 - 1)^2 \right) \right) dx + \int_{\Gamma_T, \Gamma_B} \left(BL_c(\phi) \frac{\partial \phi}{\partial t} - B \frac{\partial \gamma_{wf}^*(\phi)}{\partial t} \right) ds = 0, \tag{2.27}$$

$$\int_{\Omega} (p \nabla \cdot \mathbf{u} + \delta p^2) dx = 0, \tag{2.28}$$

$$\int_{\Omega} \left(\frac{Re}{2} \frac{\partial}{\partial t} |\mathbf{u}|^2 - p(\nabla \cdot \mathbf{u}) + |\nabla \mathbf{u}|^2 - B(\omega + c\phi) \nabla \phi \cdot \mathbf{u} \right) dx + \int_{\Gamma_T, \Gamma_B} \left(\frac{1}{L_s} u_x^{slip} (u_x^{slip} + u_w) - BL_c(\phi) \partial_x \phi u_x \right) ds = 0. \tag{2.29}$$

Then (2.26)–(2.27)+(2.28)+(2.29) yields an energy law as follows

$$\begin{aligned} \frac{dE}{dt} = & - \left(\|\nabla \mathbf{u}\|_{L^2}^2 + BL_d \|\omega + c\phi\|_{L^2}^2 + \delta \|p\|_{L^2}^2 \right) - \int_{\Gamma_T, \Gamma_B} \left(\frac{1}{L_s} u_x^{slip} u_w \right) ds \\ & - \int_{\Gamma_T, \Gamma_B} \left(BV_s |L_c(\phi)|^2 + \frac{1}{L_s} |u_x^{slip}|^2 \right) ds, \end{aligned} \quad (2.30)$$

where

$$E = \frac{Re}{2} \|\mathbf{u}\|_{L^2}^2 + \frac{B\epsilon}{2} \|\nabla \phi\|_{L^2}^2 + B \int_{\Omega} \left(\frac{1}{4\epsilon} (\phi^2 - 1)^2 \right) d\mathbf{x} + B \int_{\Gamma_T, \Gamma_B} \gamma_{wf}^*(\phi) ds,$$

is the total free energy.

The energy law (2.30) is applicable to the example in Section 4.1, but not directly to the example drop displacement in Section 4.2. For the example in Section 4.2 the energy law will be slightly modified there. Through the examples in Section 4, we will show that the total free energy (E) increases by time during the simulation where meanwhile the total energy that is the sum of total free energy and the work done to the wall (G in Section 3) decreases by time due to the second term in the right hand side of (2.30). In the next section we will present a fully discrete scheme for the NSCH system and derive a discrete energy law.

3 Fully discretized NSCH system and discrete energy laws

The solution of the weak problem (2.22)-(2.25) is approximated by a finite difference scheme in time and a conformal C^0 finite element method in space.

As usual, let

$$\mathbf{W} = \mathbf{W}^{1,3}(\Omega) \times L_0^2(\Omega) \times W^{1,3}(\Omega) \times W^{1,3}(\Omega)$$

and $\mathbf{W}^h = \mathbf{U}^h \times \mathcal{P}^h \times \mathbf{H}^h \times \mathbf{H}^h \subset \mathbf{W}$ be a finite dimensional subspace of \mathbf{W} . Further, $\Delta t > 0$ denotes the time step size, $(\mathbf{u}_h^n, p_h^n, \phi_h^n, \omega_h^n) \in \mathbf{W}^h$ is an approximation of $\mathbf{u}(t^n) = \mathbf{u}(n\Delta t)$, $p(t^n) = p(n\Delta t)$, $\phi(t^n) = \phi(n\Delta t)$ and $\omega(t^n) = \omega(n\Delta t)$, and $(\mathbf{u}_h^{n+1}, p_h^{n+1}, \phi_h^{n+1}, \omega_h^{n+1})$ is the approximation at time $t^{n+1} = (n+1)\Delta t$. The modified midpoint scheme [20,23] was able to preserve the continuous energy law accurately for a two-phase flow problem. Therefore we slightly modify it to fit the weak problem (2.22)-(2.25) and derive a discrete energy law in this section. The fully discrete system we propose reads:

$$\int_{\Omega} \left(\phi_t^{n+1} \psi + \left(\mathbf{u}_h^{n+\frac{1}{2}} \cdot \nabla \phi_h^{n+\frac{1}{2}} \right) \psi + L_d \nabla \left(\omega_h^{n+\frac{1}{2}} + c\phi_h^{n+\frac{1}{2}} \right) \cdot \nabla \psi \right) d\mathbf{x} = 0, \quad (3.1)$$

$$\int_{\Omega} \left(\left(\omega_h^{n+\frac{1}{2}} + c\phi_h^{n+\frac{1}{2}} \right) \chi - \epsilon \nabla \phi_h^{n+\frac{1}{2}} \cdot \nabla \chi - \frac{\chi}{\epsilon} g(\phi_h^{n+1}, \phi_h^n) \right) d\mathbf{x} - \int_{\Gamma_T, \Gamma_B} \left(\frac{\chi}{V_s} \left(\phi_{\bar{i}}^{n+1} + u_{h,x}^{n+\frac{1}{2}} \partial_x \phi_h^{n+\frac{1}{2}} \right) + \frac{\gamma_{wf}^*(\phi^{n+1}) - \gamma_{wf}^*(\phi^n)}{\phi^{n+1} - \phi^n} \chi \right) ds = 0, \quad (3.2)$$

$$\int_{\Omega} \left(\nabla \cdot \mathbf{u}_h^{n+\frac{1}{2}} + \delta p_h^{n+\frac{1}{2}} \right) q d\mathbf{x} = 0, \quad (3.3)$$

$$\int_{\Omega} \left(\text{Re} \left(\mathbf{u}_{\bar{i}}^{n+1} \cdot \mathbf{v} + \left(\mathbf{u}_h^{n+\frac{1}{2}} \cdot \nabla \right) \mathbf{u}_h^{n+\frac{1}{2}} \cdot \mathbf{v} \right) + \frac{\text{Re}}{2} \left(\left(\nabla \cdot \mathbf{u}_h^{n+\frac{1}{2}} \right) \mathbf{u}_h^{n+\frac{1}{2}} \right) \cdot \mathbf{v} \right) d\mathbf{x} + \int_{\Omega} \left(-p_h^{n+\frac{1}{2}} (\nabla \cdot \mathbf{v}) + \nabla \mathbf{u}_h^{n+\frac{1}{2}} : \nabla \mathbf{v} - B \left(\omega_h^{n+\frac{1}{2}} + c\phi_h^{n+\frac{1}{2}} \right) \nabla \phi_h^{n+\frac{1}{2}} \cdot \mathbf{v} \right) d\mathbf{x} + \int_{\Gamma_T, \Gamma_B} \left(\frac{1}{L_s} u_{h,x}^{slip, n+\frac{1}{2}} v_x + \frac{B}{V_s} \left(\phi_{\bar{i}}^{n+1} + u_{h,x}^{n+\frac{1}{2}} \partial_x \phi_h^{n+\frac{1}{2}} \right) \partial_x \phi_h^{n+\frac{1}{2}} v_x \right) ds = 0, \quad (3.4)$$

for all $(\psi, \chi, q, \mathbf{v}) \in \mathbf{W}^h$ where $\mathbf{u}_h = (u_{h,x}, u_{h,z})$, $u_{h,x}^{slip, n+1/2} = u_h^{n+1/2} - u_w$ (u_w represents wall speed), $\phi_{\bar{i}}^{n+1} = (\phi_h^{n+1} - \phi_h^n) / \Delta t$, $\mathbf{u}_{\bar{i}}^{n+1} = (\mathbf{u}_h^{n+1} - \mathbf{u}_h^n) / \Delta t$, $\phi_h^{n+1/2} = (\phi_h^n + \phi_h^{n+1}) / 2$, $\mathbf{u}_h^{n+1/2} = (\mathbf{u}_h^n + \mathbf{u}_h^{n+1}) / 2$, $p_h^{n+1/2} = (p_h^n + p_h^{n+1}) / 2$, $\omega_h^{n+1/2} = (\omega_h^n + \omega_h^{n+1}) / 2$ and

$$g(\phi_h^{n+1}, \phi_h^n) = \frac{(|\phi_h^{n+1}|^2 + |\phi_h^n|^2 - 2)(\phi_h^{n+1} + \phi_h^n)}{4}.$$

Similarly, if we take $\psi = B(\omega_h^{n+1/2} + c\phi_h^{n+1/2})$, $\mathbf{v} = \mathbf{u}_h^{n+1/2}$, $q = p_h^{n+1/2}$, $\chi = B\phi_{\bar{i}}^{n+1}$ in (3.1)–(3.4) and do (3.1)+(3.4)–(3.2)+(3.3), and some derivation in [29]:

$$\nabla \phi_h^{n+\frac{1}{2}} \cdot \nabla B\phi_{\bar{i}}^{n+1} = \left(\nabla \frac{\phi_h^{n+1} + \phi_h^n}{2} \right) \cdot \nabla B \frac{\phi_h^{n+1} - \phi_h^n}{\Delta t} = \frac{B}{2} \frac{(\nabla \phi_h^{n+1})^2 - (\nabla \phi_h^n)^2}{\Delta t} = \frac{B}{2} \left(|\nabla \phi_h^{n+1}|^2 \right)_{\bar{i}}, \quad (3.5)$$

$$\int_{\Omega} \left[\left(\mathbf{u}_h^{n+\frac{1}{2}} \cdot \nabla \right) \mathbf{u}_h^{n+\frac{1}{2}} \cdot \mathbf{u}_h^{n+\frac{1}{2}} + \frac{1}{2} \left(\left(\nabla \cdot \mathbf{u}_h^{n+\frac{1}{2}} \right) \mathbf{u}_h^{n+\frac{1}{2}} \right) \cdot \mathbf{u}_h^{n+\frac{1}{2}} \right] d\mathbf{x} = 0, \quad (3.6)$$

$$\left(|\phi_h^{n+1}|^2 + |\phi_h^n|^2 - 2 \right) \left(\phi_h^{n+1} + \phi_h^n \right) B\phi_{\bar{i}}^{n+1} = B \left(\left(\phi_h^{n+1} \right)^2 - 1 \right)_{\bar{i}}, \quad (3.7)$$

$$\frac{\gamma_{wf}^*(\phi_h^{n+1}) - \gamma_{wf}^*(\phi_h^n)}{\phi_h^{n+1} - \phi_h^n} B\phi_{\bar{i}}^{n+1} = B \frac{\gamma_{wf}^*(\phi_h^{n+1}) - \gamma_{wf}^*(\phi_h^n)}{\phi_h^{n+1} - \phi_h^n} \frac{\phi_h^{n+1} - \phi_h^n}{\Delta t} = B\gamma_{wf}^*(\phi_h^{n+1})_{\bar{i}}, \quad (3.8)$$

we can obtain a discrete energy law:

$$E^{n+1} - E^n = -\Delta t \left(\|\nabla \mathbf{u}_h^{n+\frac{1}{2}}\|_{L^2}^2 + BL_d \|\omega_h^{n+\frac{1}{2}} + c\phi_h^{n+\frac{1}{2}}\|_{L^2}^2 + \delta \|p_h^{n+\frac{1}{2}}\|_{L^2}^2 \right) - G^{n+1} + G^n - \int_{\Gamma_T, \Gamma_B} \Delta t \left(\frac{B}{V_s} |\phi_{\bar{i}}^{n+1} + u_{h,x}^{n+\frac{1}{2}} \partial_x \phi_h^{n+\frac{1}{2}}|^2 + \frac{1}{L_s} |u_{h,x}^{slip, n+\frac{1}{2}}|^2 \right) ds, \quad (3.9)$$

where

$$E^i = \frac{Re}{2} \|\mathbf{u}_h^i\|_{L^2}^2 + \frac{B\epsilon}{2} \|\nabla \phi_h^i\|_{L^2}^2 + B \int_{\Omega} \left(\frac{1}{4\epsilon} \left((\phi_h^i)^2 - 1 \right)^2 \right) d\mathbf{x} + B \int_{\Gamma_T, \Gamma_B} \gamma_{wf}^* (\phi_h^i) ds, \quad (3.10)$$

$$G^i = \sum_{k=0}^{i-1} \int_{\Gamma_T, \Gamma_B} \Delta t \left(\frac{1}{L_s} u_{h,x}^{slip, k+\frac{1}{2}} u_w \right) ds, \quad (3.11)$$

and G represents the work done to the wall in [19].

It is indicated in [20] that the midpoint scheme may cause oscillation near the interface due to the stiffness associated with (2.21). Therefore we adopt the remedy in [20], where we use a stiffly stable scheme (e.g. backward Euler scheme) at the first time step and use the modified midpoint scheme (3.1)-(3.4) afterwards.

This discrete scheme is nonlinear implicit, therefore we need to introduce a linearization and an iterative method at each time step. As in [20, 23] we apply a fixed point method in the linearization process. We can also use Newton method which converges much faster than a fixed point method at each time step. But the linear system resulted from Newton method depends on the time, which increases the computation cost. The resulted linear system by a carefully designed fixed point method may not depend on the time and we just need to do the LU factorization of the linear system once at the initial two time steps. So it is efficient in the time evolution. If the fixed point method does not converge, then we have to replace it by the Newton method.

The following iterative scheme (for $s=1, 2, \dots$) is used at every time level t^{n+1} , i.e. find $\bar{\phi}_s$, $\bar{\omega}_s$, $\bar{\mathbf{u}}_s$ and \bar{p}_s (as an approximation of ϕ_h^{n+1} , ω_h^{n+1} , \mathbf{u}_h^{n+1} and p_h^{n+1} , respectively) to satisfy:

$$\begin{aligned} & \int_{\Omega} \left(\frac{\bar{\phi}_s - \phi_h^n}{\Delta t} \psi + \left(\frac{\bar{\mathbf{u}}_{s-1} + \mathbf{u}_h^n}{2} \cdot \nabla \frac{\bar{\phi}_{s-1} + \phi_h^n}{2} \right) \psi \right. \\ & \left. + L_d \nabla \left(\frac{\bar{\omega}_s + \omega_h^n}{2} + c \frac{\bar{\phi}_s + \phi_h^n}{2} \right) \cdot \nabla \psi \right) d\mathbf{x} = 0, \end{aligned} \quad (3.12)$$

$$\begin{aligned} & \int_{\Omega} \left(\left(\frac{\bar{\omega}_s + \omega_h^n}{2} + c \frac{\bar{\phi}_s + \phi_h^n}{2} \right) \chi - \epsilon \nabla \left(\frac{\bar{\phi}_s + \phi_h^n}{2} \right) \cdot \nabla \chi - \frac{\chi}{4\epsilon} (|\bar{\phi}_{s-1}|^2 + |\phi_h^n|^2 - 2) \right. \\ & \left. \times (\bar{\phi}_{s-1} + \phi_h^n) \right) d\mathbf{x} - \int_{\Gamma_T, \Gamma_B} \left(\frac{\chi}{V_s} \left(\frac{\bar{\phi}_s - \phi_h^n}{\Delta t} + \frac{\bar{u}_{s-1,x} + u_{h,x}^n}{2} \partial_x \left(\frac{\bar{\phi}_{s-1} + \phi_h^n}{2} \right) \right) \right. \\ & \left. - \frac{\sqrt{2}}{3} \cos \theta_s^{surf} \frac{\sin(\frac{\pi}{2} \bar{\phi}_{s-1}) - \sin(\frac{\pi}{2} \phi_h^n)}{\bar{\phi}_{s-1} - \phi_h^n} \chi \right) ds = 0, \end{aligned} \quad (3.13)$$

$$\int_{\Omega} \left(\nabla \cdot \frac{\bar{\mathbf{u}}_s + \mathbf{u}_h^n}{2} + \delta \frac{\bar{p}_s + p_h^n}{2} \right) q d\mathbf{x} = 0, \quad (3.14)$$

$$\begin{aligned}
& \int_{\Omega} \left(Re \left(\frac{\bar{\mathbf{u}}_s - \mathbf{u}_h^n}{\Delta t} \cdot \mathbf{v} + \left(\frac{\bar{\mathbf{u}}_{s-1} + \mathbf{u}_h^n}{2} \cdot \nabla \right) \frac{\bar{\mathbf{u}}_{s-1} + \mathbf{u}_h^n}{2} \cdot \mathbf{v} \right) + \frac{Re}{2} \left(\left(\nabla \cdot \frac{\bar{\mathbf{u}}_{s-1} + \mathbf{u}_h^n}{2} \right) \right. \right. \\
& \quad \times \left. \left. \frac{\bar{\mathbf{u}}_{s-1} + \mathbf{u}_h^n}{2} \right) \cdot \mathbf{v} - \frac{\bar{p}_s + p_h^n}{2} (\nabla \cdot \mathbf{v}) + \nabla \frac{\bar{\mathbf{u}}_s + \mathbf{u}_h^n}{2} : \nabla \mathbf{v} - B \left(\frac{\bar{\omega}_{s-1} + \omega_h^n}{2} \right. \right. \\
& \quad \left. \left. + c \frac{\bar{\phi}_{s-1} + \phi_h^n}{2} \right) \nabla \frac{\bar{\phi}_{s-1} + \phi_h^n}{2} \cdot \mathbf{v} \right) d\mathbf{x} + \int_{\Gamma_T, \Gamma_B} \left(\frac{B}{V_s} \left(\frac{\bar{\phi}_{s-1} - \phi_h^n}{\Delta t} + \frac{\bar{u}_{s-1,x} + u_{h,x}^n}{2} \right. \right. \\
& \quad \left. \left. \times \partial_x \left(\frac{\bar{\phi}_{s-1} + \phi_h^n}{2} \right) \right) \partial_x \left(\frac{\bar{\phi}_{s-1} + \phi_h^n}{2} \right) v_x + \frac{1}{L_s} \frac{\bar{u}_{s,x}^{slip} + u_{h,x}^{slip,n}}{2} v_x \right) ds = 0, \quad (3.15)
\end{aligned}$$

where we choose the initial iteration as $\bar{\phi}_0 = \phi_h^n$, $\bar{\omega}_0 = \omega_h^n$, $\bar{\mathbf{u}}_0 = \mathbf{u}_h^n$ and $\bar{p}_0 = p_h^n$.

As the iterative scheme shows, we can solve (3.12) and (3.13) first to get $\bar{\phi}_s$ and $\bar{\omega}_s$ and then substitute them into (3.14) and (3.15) to obtain $\bar{\mathbf{u}}_s$ and \bar{p}_s . This will reduce computational cost significantly than solving (3.12)-(3.15) all together at the same time.

4 Numerical examples and results

In this section, to demonstrate the method presented earlier, we compute the same examples given in [19,25], i.e., immiscible fluids in a pipe and droplet displacement under the effect of pressure driven shear flow. Also the energy and the error in the energy law will be shown during the computations. The computations are carried out and the results are shown with the help of the freefem++ platform ([18]), MATLAB and Tecplot. All computations are carried out under the P_2 (piecewise polynomial of degree two) finite element space for the velocity \mathbf{u} and the phase variables ϕ and ω , and the P_1 finite element space for the pressure p . In all examples, the density and viscosity are constant. Moreover, we demonstrate that the energy law preserving method works well under a relatively coarse mesh.

4.1 Two immiscible fluids in a pipe

Some of the numerical examples in [19] are re-computed in this section. The energy and the error in the energy law are computed by using (3.9)-(3.11). Two immiscible fluids are distributed at the left and right parts of a pipe and θ_s^{surf} means the right static contact angle between the interface of fluids and the lower wall at initial time. Three cases $\theta_s^{surf} = 77.6^\circ$, $\theta_s^{surf} = 90^\circ$, $\theta_s^{surf} = 120^\circ$ are discussed. The computational domain is $[x,z] \in [0,1] \times [0,0.4]$ and 32×16 grid is used to solve the system. The upper wall speed $u_w = 1.0$ and the lower wall speed $u_w = -1.0$. Values of other parameters are:

$$L_d = 5 \times 10^{-4}, \quad Re = 3, \quad B = 12, \quad V_s = 500, \quad L_s = 0.0038, \quad \epsilon = 0.01, \quad c = 0.5 \quad \text{and} \quad \Delta t = 10^{-5}.$$

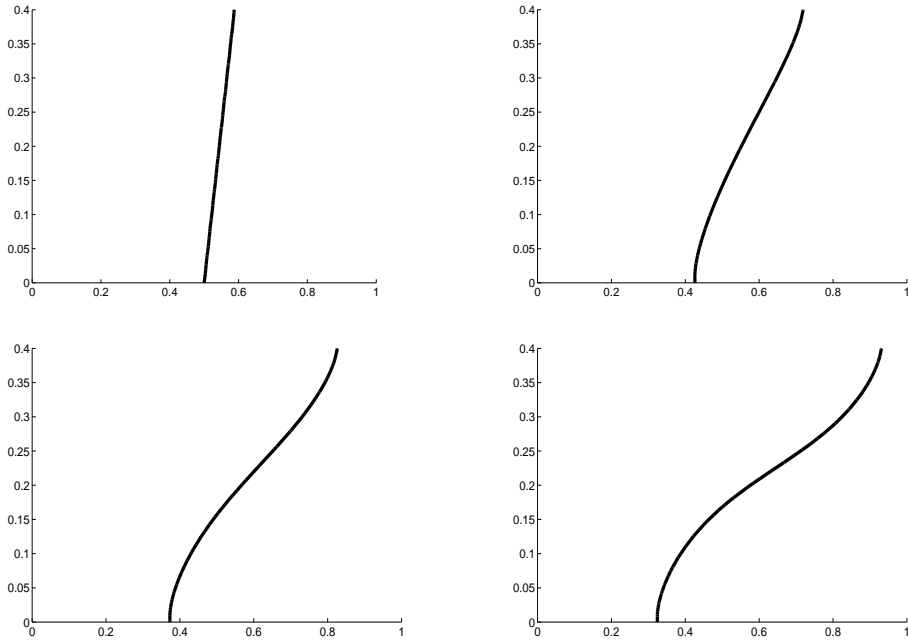


Figure 1: Deformed interfaces at the first time step, $t=0.2, 0.4$ and 0.6 for $\theta_s^{surf} = 77.6^\circ$.

The initial value of phase field parameter ϕ is

$$\phi(x, z, 0) = \tanh\left(\left(z - \tan\left(\theta_s^{surf}\right)(x - 0.5)\right) / \left(2\sqrt{2}\epsilon\right)\right).$$

Fig. 1 shows the level curves of $\phi=0$ at times $t=0, 0.2, 0.4, 0.6$ for $\theta_s^{surf} = 77.6^\circ$. The velocity along the lower boundary at time $t = 0.5938$ is depicted in Fig. 4, where we can see that the phenomena of near complete slip around contact line. Fig. 2 and Fig. 3 show the level curves at time $t = 0, 0.04, 0.12, 0.2$ for $\theta_s^{surf} = 90^\circ$, $\theta_s^{surf} = 120^\circ$, respectively. In order to show the accuracy of our scheme, we compare the result of the example in [19], where $\epsilon = 0.001$ and $u_w = \pm 0.2$ with our results. As it is shown in Fig. 5, our results are close to that of Fig. 2a in [19], where, for both examples, the position of the intersection point between the interface and the lower boundary is around 0.44 and velocities along the lower wall are very close (the smallest velocities are close to $u_x = -0.02$ and the biggest velocities are close to $u_x = -0.17$). We also observe slight difference with interface profile: the interface in [19] is a straight line, whereas the interface in our computation is slightly bending which is probably due to the relatively coarse grid in our computation. Comparing between Fig. 4 and Fig. 5, we observe that as the velocity increases the interface moves further and changes severer.

The error in the energy law and the energy are depicted in Fig. 6, where E stands for the total free energy and $E+G$ is the total energy as shown in Section 3. The figure

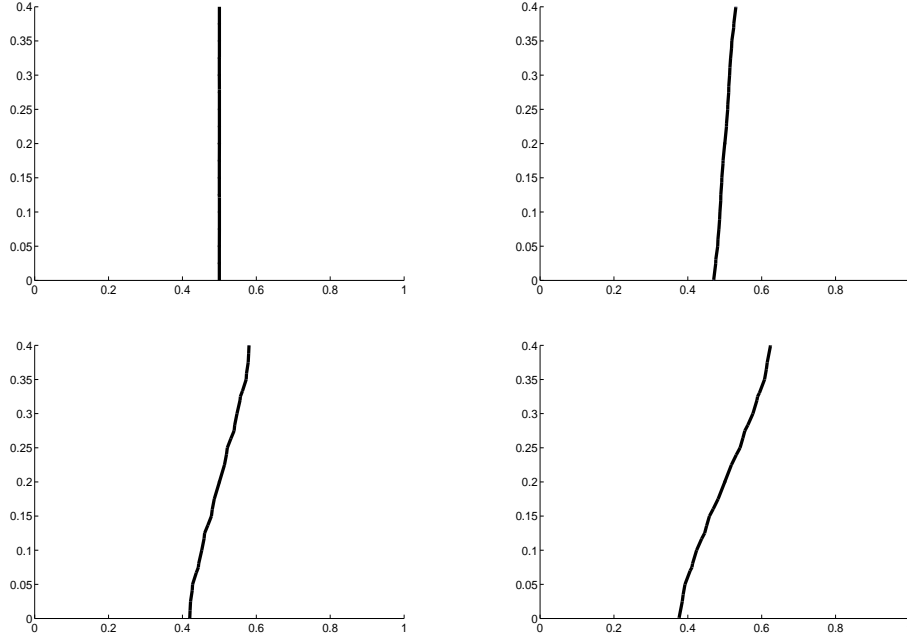


Figure 2: Deformed interfaces at the first time step, $t=0.04, 0.12$ and 0.2 for $\theta_s^{surf} = 90^\circ$.

shows the same behavior as that in [19], where the total free energy increases by time whereas the total energy decrease. The error in the energy law with an order of magnitudes $\mathcal{O}(10^{-4})$ depends on the tolerance chosen in the fixed point iterative method and seems to be good enough for the computation. The energies for $\theta_s^{surf} = 120^\circ$ have the same behavior. If we want to obtain a smoother interface in Fig. 1, we can use a finer grid (e.g. a 64×32 grid). Certainly a finer grid will cost more computational time.

To determine roughly the accuracy of the method we compute $\|\nabla \cdot (\mathbf{u} - \mathbf{u}_h^n)\| = \|\nabla \cdot \mathbf{u}_h^n\| = (\int_\Omega |\nabla \cdot \mathbf{u}_h^n|^2 dx)^{1/2}$ at a time step. The estimated order of the finite element method for $\nabla \cdot \mathbf{u}$ is computed as $\lg(\|\nabla \cdot (\mathbf{u} - \mathbf{u}_h)\| / \|\nabla \cdot (\mathbf{u} - \mathbf{u}_{h/2})\|) / \lg 2$, which can be more than one as indicated in Table 1.

Table 1: The estimated order for $\nabla \cdot \mathbf{u}$ with $\theta_s^{surf} = 77.6^\circ$.

mesh	32x16	64x32	128x64
$\ \nabla \cdot (\mathbf{u} - \mathbf{u}_h)\ $	0.163548	0.0837296	0.0319579
estimated order	-	0.96	1.39

As it is discussed in [34], the sharp-interface limit for the phase field model based on moving contact line problems can be achieved by reducing the thickness of interface ϵ , with the criterion $\epsilon < 4l_d = 4\sqrt{L_d/B}$. In [34], the no slip boundary condition for the

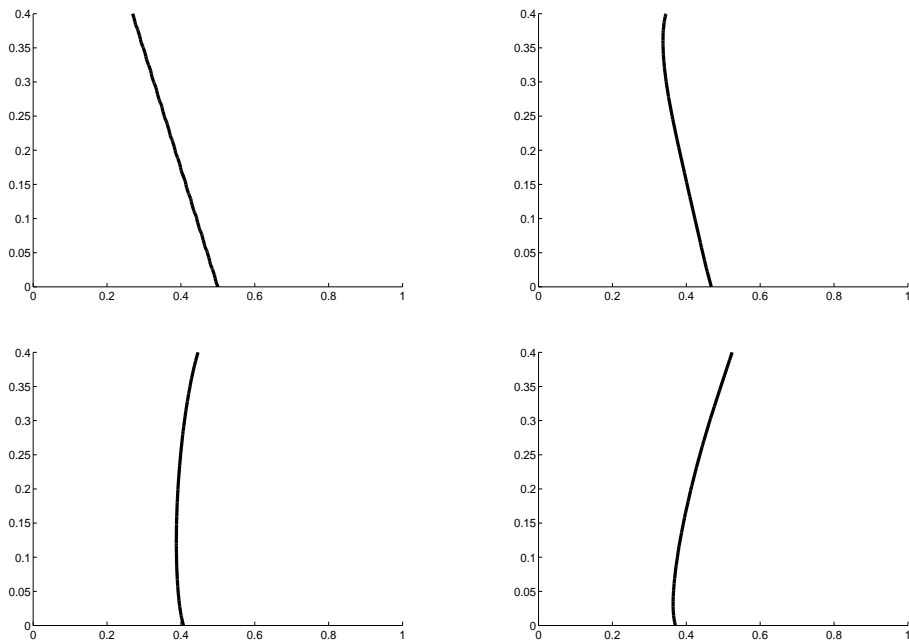


Figure 3: Deformed interfaces at the first time step, $t=0.04, 0.12$ and 0.2 for $\theta_s^{surf} = 120^\circ$.

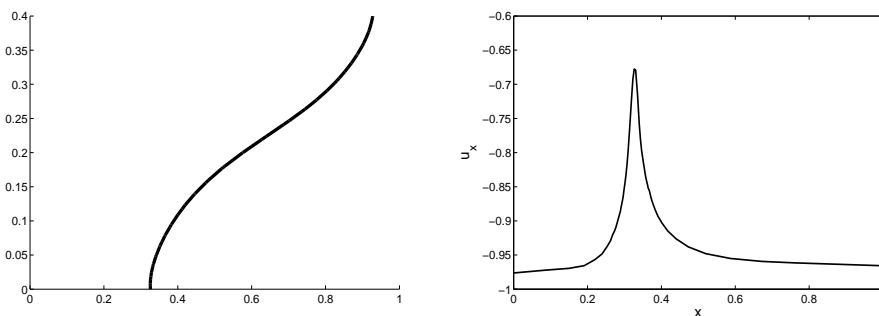


Figure 4: Interfaces structure and the u_x along lower boundary at $t=0.5938$ for $\theta_s^{surf} = 77.6^\circ$, $\epsilon = 0.01$ and $u_w = \pm 1.0$.

velocity is adopted and $L_s = 2.5l_d$, where L_s is the slip length, l_d is the diffusion length. In the present work, the phase field model and slip condition GNBC are adopted where both of l_d and L_s exist. Therefore, except the relation $L_s = 2.5l_d$, there are various choices of relations between l_d and L_s can be adopted. Moreover, if L_s arbitrarily chosen, the criterion ($\epsilon < 4l_d$) may not be suitable for the model in the present work. To demonstrate this viewpoint, we re-compute the first case ($\theta_s^{surf} = 77.6^\circ$) in Section 4.1, where we have $l_d = \sqrt{L_d/B} = 0.0065$ whereas $L_s = 0.0038 \neq 2.5l_d$. Three values of interface thickness ϵ ,

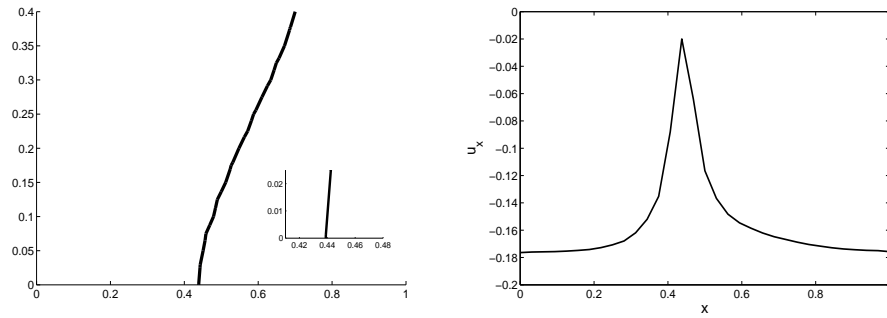


Figure 5: Interfaces structure and the u_x along lower boundary at $t = 0.5938$ for $\theta_s^{surf} = 77.6^\circ$, $\epsilon = 0.001$ and $u_w = \pm 0.2$.

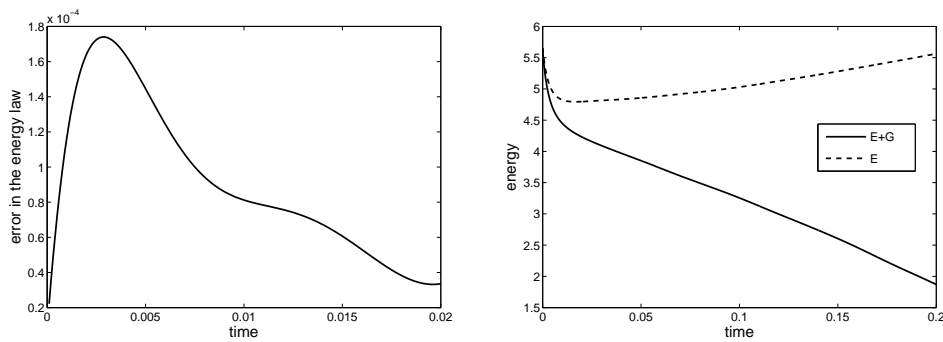


Figure 6: Left: The error ($\approx \mathcal{O}(10^{-4})$) in the energy law; Right: The total energy and total free energy, when $\theta_s^{surf} = 90^\circ$ and $\Delta t = 0.00001$.

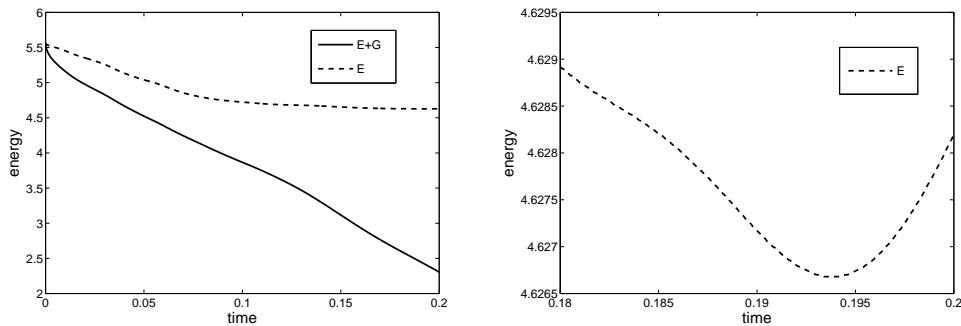


Figure 7: The total free energy and total energy when $\theta_s^{surf} = 120^\circ$.

$\epsilon = 0.02$, $\epsilon = 0.01$ and $\epsilon = 0.005$, are chosen to show the interfaces structure at $t = 0.12$ and all the thickness satisfy the criterion ($\epsilon < 4l_d$). Fig. 8 shows that for $L_s = 0.0038$ (left) the interfaces converge to a unique shape for the case $\epsilon = 0.01$ and $\epsilon = 0.005$, but not for $\epsilon = 0.02$. However if we set $L_s = 2.5l_d = 0.01625$ (right), three interfaces with different

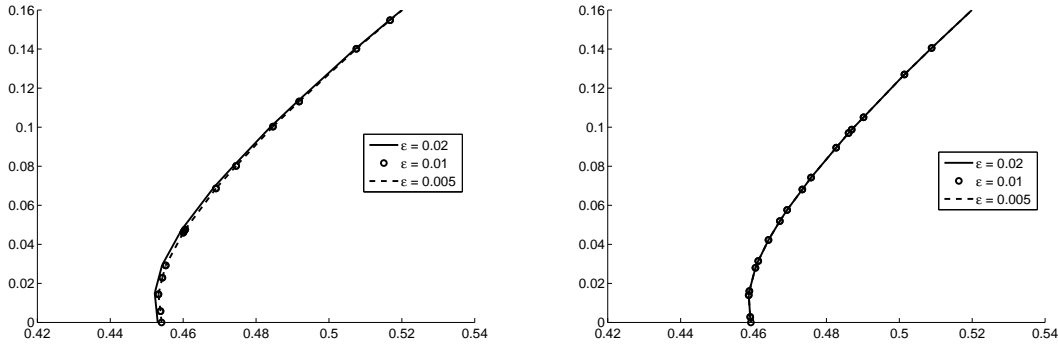


Figure 8: The compare of three groups of interface thickness. Left: $L_s = 0.0038$; Right: $L_s = 0.01625$.

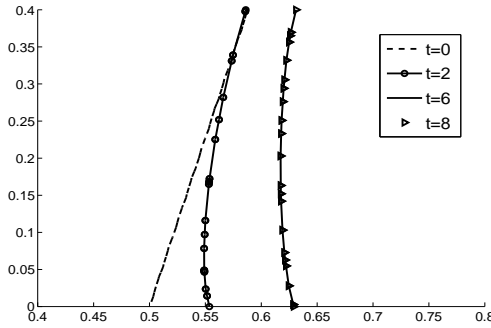


Figure 9: Deformed interfaces at time $t=0$, $t=2$, $t=6$ and $t=8$ for $\theta_s^{surf} = 77.6^\circ$ and $u_w = 0$.

interface thicknesses all converge to a unique shape. It means that for Cahn-Hilliard model based on GNBC, the criterion ($\epsilon < 4l_d$) may not be suitable for the sharp-interface limit if the slip length L_s is arbitrary chosen. But the results in Fig. 8 show that this slip model also has the sharp-interface limit for any slip length.

We also compute the example of still walls ($u_w = 0$), where we set $\theta_s^{surf} = 77.6^\circ, 90^\circ$ and 120° respectively. As shown in Figs. 9-11, the interface is a straight line for three cases at the initial time. For the case $\theta_s^{surf} = 90^\circ$, the interface stays steady for all the time, whereas for the case $\theta_s^{surf} \neq 90^\circ$, the interface turns to be a parabolic shape at the steady state.

4.2 The droplet displacement under the effect of pressure driven shear flow

A simulation based on a relatively large L_d and a suitably chosen V_s can make the numerical solution much closer to the solution in a moving-contact-line experiment with a much smaller slip length [35]. Imposing the dynamics contact angle can result in an accurate macroscopic solution effectively and the large V_s returns the dynamics contact angle

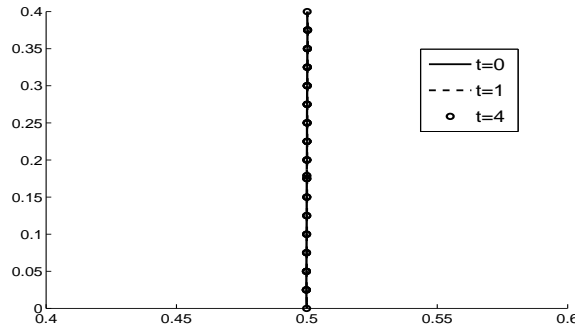


Figure 10: Deformed interfaces at time $t=0$, $t=1$ and $t=4$ for $\theta_s^{surf} = 90^\circ$ and $u_w = 0$.

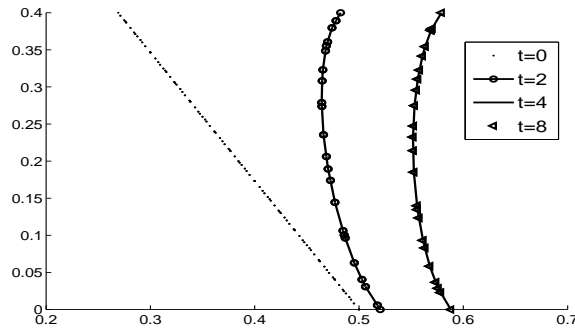


Figure 11: Deformed interfaces at time $t=0$, $t=2$, $t=4$ and $t=8$ for $\theta_s^{surf} = 120^\circ$ and $u_w = 0$.

to the equilibrium static contact angle. The same situation is also discussed in [36–38]. We choose several large V_s in our numerical examples and we do not impose dynamics contact angle in this paper.

In this section, we re-compute the example of a droplet displacement under the effect of a pressure driven shear flow [25]. The energy law for this example is slightly different from (2.30) which is due to the new boundary condition. At the initial time, the fluid is at rest and there is a droplet in connection with the lower boundary. The pressure p_l on the left boundary and p_r on the right boundary maintain a difference ($p_l - p_r = 1000$) for all the time. The fluid flows then under the pressure difference and the droplet moves under the effect of the shear flow. The computing domain is $[x, z] \in [0, 1.2] \times [0, 0.6]$. The values of parameters are the same as those in [25]:

$$Re = 5, \quad L_s = 0.0025, \quad \epsilon = 0.003, \quad B = 12, \quad V_s = 200, \quad L_d = 5 \times 10^{-4}, \quad c = 0.5.$$

Three cases $\theta_s^{surf} = 60^\circ$, $\theta_s^{surf} = 90^\circ$ and $\theta_s^{surf} = 120^\circ$ are discussed and the similar results as in [25] are shown in Figs. 12, 13 and 14 respectively. The finite element grid 64×32 and time step $\Delta t = 10^{-5}$ is adopted for the former two cases and grid 128×64 , $\Delta t = 10^{-6}$ for

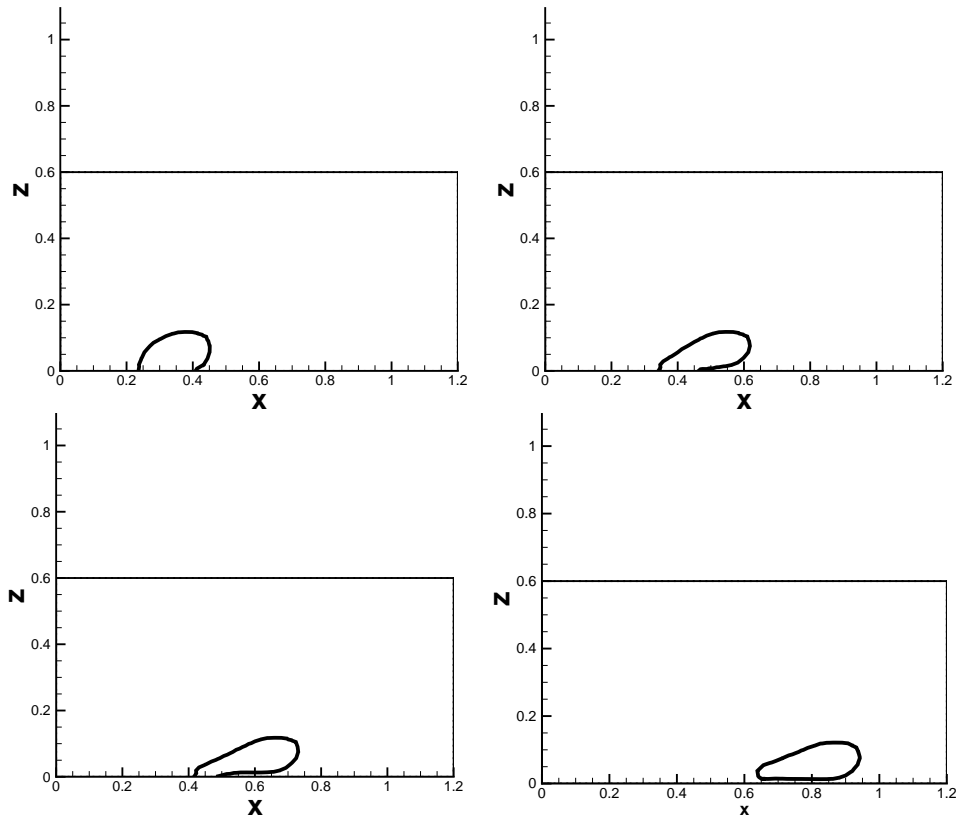


Figure 12: The interface structure of droplet displacement with $\theta_s^{surf} = 60^\circ$ at $t=0.04, 0.08, 0.12$ and 0.20 .

the last case. In fact our static angle is the supplementary angle in [25]. Here the weak form of the momentum equation has to be slightly modified as the fluid flow is driven by the pressure difference. The modified weak form for the momentum equations reads:

$$\int_{\Omega} \left(Re \left(\frac{\partial \mathbf{u}}{\partial t} \cdot \mathbf{v} + (\mathbf{u} \cdot \nabla) \mathbf{u} \cdot \mathbf{v} \right) - p(\nabla \cdot \mathbf{v}) + \nabla \mathbf{u} : \nabla \mathbf{v} - B(\omega + c\phi) \nabla \phi \cdot \mathbf{v} \right) dx + \int_{\Gamma_T, \Gamma_B} \left(\frac{1}{L_s} u_x^{slip} v_x - BL_c(\phi) \partial_x \phi v_x \right) ds + \int_{\Gamma_L, \Gamma_R} (p \mathbf{v} \cdot \mathbf{n}) ds = 0. \quad (4.1)$$

The initial value of ϕ is

$$\phi(x, z, 0) = \tanh \left(\left(\sqrt{(x-0.3)^2 + z^2} - 0.1 \right) / (2\sqrt{2}\epsilon) \right).$$

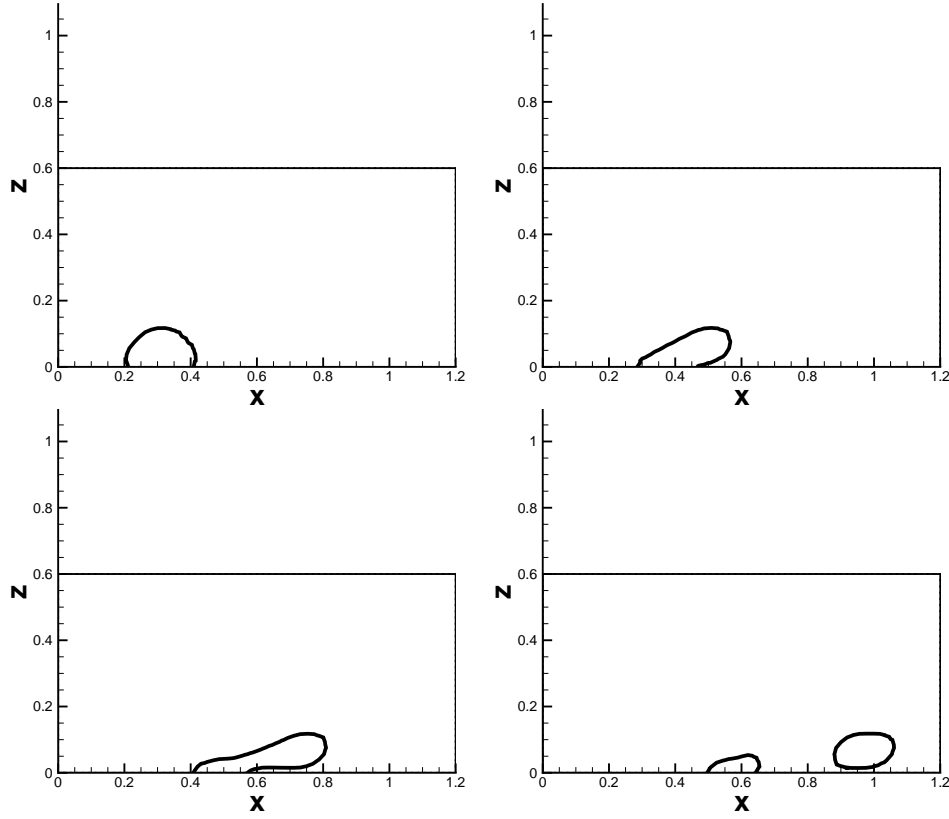


Figure 13: The interface structure of droplet displacement with $\theta_s^{surf} = 90^\circ$ at $t=0.04, 0.08, 0.20$ and 0.24 .

Comparing to (2.30), the energy law for this example is slightly different which becomes

$$\begin{aligned} \frac{dE}{dt} = & - \left(\|\nabla \mathbf{u}\|_{L^2}^2 + BL_d \|\omega + c\phi\|_{L^2}^2 + \delta \|p\|_{L^2}^2 \right) - \int_{\Gamma_T, \Gamma_B} \left(\frac{1}{L_s} u_x^{slip} u_w \right) ds \\ & - \int_{\Gamma_T, \Gamma_B} \left(BV_s |L_c(\phi)|^2 + \frac{1}{L_s} |u_x^{slip}|^2 \right) ds - \int_{\Gamma_L, \Gamma_R} \frac{Re}{2} (|\mathbf{u}|^2 \mathbf{u} \cdot \mathbf{n}) ds - \int_{\Gamma_L, \Gamma_R} (p \mathbf{u} \cdot \mathbf{n}) ds, \end{aligned} \quad (4.2)$$

and the discrete energy law for the droplet displacement is:

$$\begin{aligned} E^{n+1} - E^n = & -\Delta t \left(\|\nabla \mathbf{u}_h^{n+\frac{1}{2}}\|_{L^2}^2 + BL_d \|\omega_h^{n+\frac{1}{2}} + c\phi_h^{n+\frac{1}{2}}\|_{L^2}^2 + \delta \|p_h^{n+\frac{1}{2}}\|_{L^2}^2 \right) - G^{n+1} + G^n \\ & - \int_{\Gamma_T, \Gamma_B} \Delta t \left(\frac{B}{V_s} |\phi_i^{n+1} + u_{h,x}^{n+\frac{1}{2}} \partial_x \phi_h^{n+\frac{1}{2}}|^2 + \frac{1}{L_s} |u_{h,x}^{slip, n+\frac{1}{2}}|^2 \right) ds - \int_{\Gamma_R} \Delta t \left(\frac{Re}{2} \left(u_{h,x}^{n+\frac{1}{2}} \right)^3 \right. \\ & \left. + p_h^{n+\frac{1}{2}} u_{h,x}^{n+\frac{1}{2}} \right) ds + \int_{\Gamma_L} \Delta t \left(\frac{Re}{2} \left(u_{h,x}^{n+\frac{1}{2}} \right)^3 + p_h^{n+\frac{1}{2}} u_{h,x}^{n+\frac{1}{2}} \right) ds, \end{aligned} \quad (4.3)$$

where E^i and G^i are given in (3.10) and (3.11). The continuous and discrete energy laws

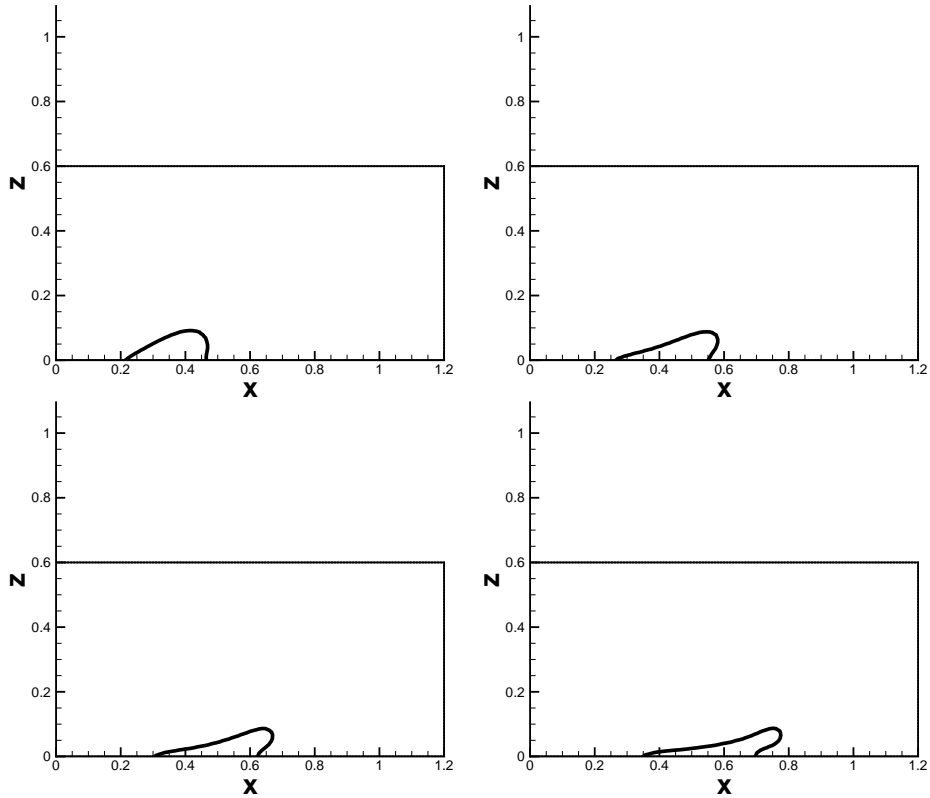


Figure 14: The interface structure of droplet displacement with $\theta_s^{surf} = 120^\circ$ at $t = 0.04, 0.10, 0.16$ and 0.20 .

are slightly different in this example. As the droplet spreads under the effect of pressure difference, the immiscible fluids flow in one direction from left to right. The flow is not Couette flow any more and we don't have the boundary condition $u_x(x, z) = -u_x(x, -z)$, which together with the work done by the pressure difference across the pipe formulate additional terms in the energy law of this example (the last two terms in (4.2)).

From the figures we can see that the results of these three cases are similar to the results in [25]. When $\theta_s^{surf} = 60^\circ$, the droplet moves along the lower wall at first, and eventually moves off the lower wall. In other words, the whole droplet pinches off. When $\theta_s^{surf} = 90^\circ$, the droplet first moves along the lower wall as well and later its upper portion pinches off. When $\theta_s^{surf} = 120^\circ$, no pinch-off can be observed. As our static angle is the supplementary angle in [25], the phenomenon of pinch-off confirms the assertion in [26, 27], which states that the increase of the contact angle results in a larger fraction of droplet being entrained in the bulk. The energy and the error in the energy law in Fig. 15 show the accuracy of the discrete energy law. Even though the energy law is different from the one in Section 4.1, the energy and error in the energy law for the other two cases behave similarly.

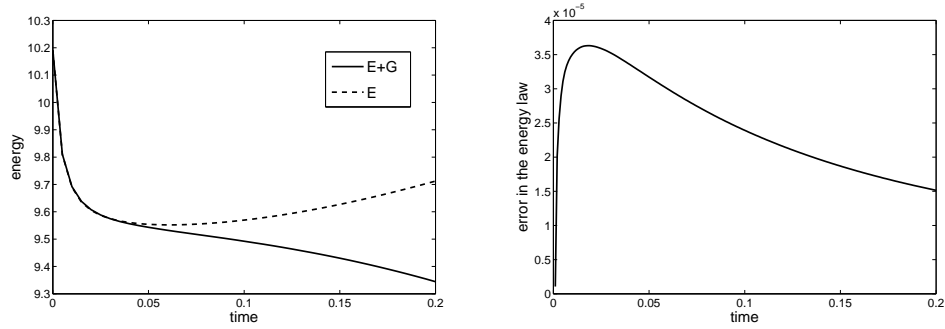


Figure 15: The total free energy (E), the total energy (E+G) and the error in the energy law for the droplet with example with $\theta_s^{surf} = 120^\circ$.

In addition, we compute another example to show the effect of dimensionless wall relaxation V_s on the droplet spread. Here we redefine the domain as $[x,z] \in [-0.5,0.5] \times [-0.1,0.1]$. The initial value of phase variable ϕ is set as

$$\phi = \tanh \left(\left(\sqrt{(x+0.2)^2 + (z+0.1)^2} - 0.1 \right) / (2\sqrt{2}\epsilon) \right).$$

Three groups of dimensionless wall relaxation V_s , $V_s = 100$, $V_s = 150$ and $V_s = 200$, are chosen. The result in Fig. 16 shows that a smaller V_s results in a slower drop spread which agrees with the conclusion from [35] that the drop spreads more slowly when wall relaxation increases the dynamics contact angle. The results above show that we can use this continuous finite element scheme to compute moving contact line problems with a grid as coarse as 32×16 . By reducing the grid size we find that the scheme is convergent with an estimated order in the velocity being possibly larger than one. Also the energetical stability of this scheme for moving contact line problems is directly resulted from the discrete energy law. The stability of the scheme is also demonstrated from numerical examples.

5 Conclusion

In this paper, a modified midpoint scheme in time and a continuous finite element method in space have been designed and used to compute the phase field model of Cahn-Hilliard equation coupled with Navier-Stokes equations based on GNBC for moving contact line problems. The main results of this paper can be summarized as follows,

(a) We have derived discrete energy laws which are analogous to ones in the continuous level for Couette flow and droplet displacement cases with moving contact line problems by using a continuous finite element scheme. To the best of our knowledge, these discrete energy laws by using this finite element scheme for moving contact line have not been derived before.

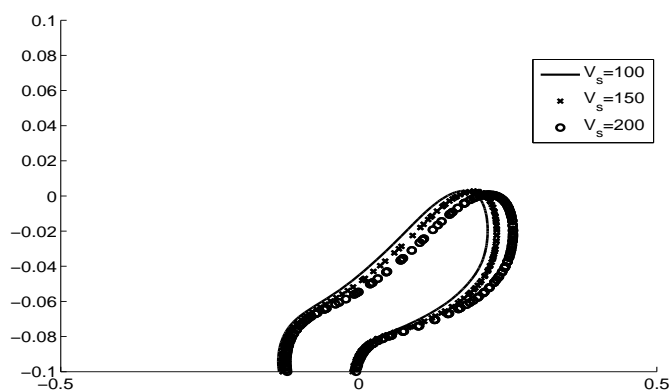


Figure 16: The compare of three groups of dimensionless wall relaxation.

(b) The numerical results obtained by our energy law preserving numerical method with a relatively coarse grid are close to the results obtained by using much finer grids [19, 25]. In addition, with a relatively coarse grid, our computations can be more effectively.

(c) The sharp-interface limit of Cahn-Hilliard model based on GNBC for moving contact line problems has been examined numerically. We show that this model truly approaches a sharp-interface limit and it can be achieved by reducing the thickness of interface. However the criterion in [34] is not suitable for this model if the slip length is arbitrarily chosen.

In future work, we plan to provide more detailed study of the moving contact line problems, e.g., to impose the dynamics contact angle. For the phase field model based on GNBC, we will also provide theoretical and numerical analysis of criterion for the sharp-interface limit where the slip length can be arbitrarily chosen.

Acknowledgments

Zhenlin Guo is partially supported by the 150th Anniversary Postdoctoral Mobility Grants (2014-15 awards) and the reference number is PMG14-15 09. Shuangling Dong is supported by the National Natural Science Foundation of China (No. 51406098). And also thank the China Postdoctoral Science Foundation (No. 2014M560967).

References

- [1] T. Qian, X. P. Wang, P. Sheng, Molecular scale contact line hydrodynamics of immiscible flows, *Phys. Rev. E*, 68 (2003), 016306.
- [2] L. Zhang, J. Aoki and B. G. Thomas, Inclusion removal by bubble floatation in a continuous casting mold, *Metall. Mater. Trans. B*, 37B (2006), 361-379.

- [3] C. E. Norman and M. J. Miksis, Gas bubble with a moving contact line rising in an inclined channel at finite Reynolds number, *Physica D*, 209 (2005), 191-204.
- [4] X. Luo, X. P. Wang, T. Qian and P. Sheng, Moving contact line over undulating surfaces, *Solid State Commun.*, 139 (2006), 623-629.
- [5] Y. Chen, R. Mertz, R. Kulenovic, Numerical simulation of bubble formation on orifice plates with a moving contact line, *Int. J. Multiphase Flow*, 35 (2009), 66-77.
- [6] J. Fuentes and R. L. Cerro, Surface forces and inertial effects on moving contact lines, *Chem. Eng. Sci.*, 62 (2007), 3231-3241.
- [7] V. S. Nikolayev, S. L. Gavrilyuk and H. Gouin, Modeling of the moving deformed triple contact line influence of the fluid inertia, *J. Colloid Interface Sci.*, 302 (2006), No. 2, pp. 605-612.
- [8] S. Zahedi, K. Gustavsson and G. Kreiss, A conservative level set method for contact line dynamics, *J. Comput. Phys.*, 228 (2009), No. 17, pp. 6361-6375.
- [9] J. F. Gerbeau and T. Lelivre, Generalized Navier boundary condition and geometric conservation law for surface tension, *Comput. Methods Appl. Mech. Engrg.*, 198 (2009), 644-656.
- [10] X. M. Xu and X. P. Wang, Derivation of the wenzel and cassie equation from a phase field model for two phase flow on rough surface, *SIAM J. APPL. MATH.* 70 (2010), 2929-2941.
- [11] D. Jacqmin, Contact line dynamics of a diffuse fluid interface, *J. Fluid Mech.*, 402 (2000), 57-88.
- [12] P. Seppecher, Moving contact lines in the Cahn-Hilliard theory, *Int. J. Eng. Sci.*, 34 (1996), 977-992.
- [13] Z. Li, M. C. Lai, G. He and H. Zhao, An augmented method for free boundary problems with moving contact lines, *Comput. Fluids*, 39 (2010), 1033-1040.
- [14] Q. He, R. Glowinski and X. P. Wang, A least-squares/finite element method for the numerical solution of the Navier-Stokes-Cahn-Hilliard system modeling the motion of the contact line, *J. Comput. Phys.*, 230 (2011), 4991-5009.
- [15] M. Renardy, Y. Renardy and J. Li, Numerical simulation of moving contact line problems using a volume-of-fluid method, *J. Comput. Phys.*, 171 (2001), 243-263.
- [16] N. G. Hadjiconstantinou, Hybrid atomistic-continuum formulations and the moving contact-line problem, *J. Comput. Phys.*, 154 (1999), 245-265.
- [17] J. Shen and X. Yang, An efficient moving mesh spectral method for the phase-field model of two-phase flows, *J. Comput. Phys.*, 228 (2009), 2978-2992.
- [18] F. Hecht, O. Pironneau, A. Le Hyaric and K. Ohtsuka, *FreeFem++* (Version 2.17-1), 2007 (<http://www.freefem.org/ff++/ftp/freefem++doc.pdf>).
- [19] M. Gao and X. P. Wang, A gradient stable scheme for a phase field model for the moving contact line problem, *J. Comput. Phys.*, 231 (2012), 1372-1386.
- [20] J. Hua, P. Lin, C. Liu and Q. Wang, Energy law preserving C^0 finite element schemes for phase field models in two-phase flow computations, *J. Comput. Phys.*, 230 (2011), 7115-7131.
- [21] T. Qian, X. P. Wang and P. Sheng, A variational approach to the moving contact line hydrodynamics, *J. Fluid Mech.*, 564 (2006), 333-360.
- [22] P. Lin and C. Liu, Simulation of singularity dynamics in liquid crystal flows: A C^0 finite element approach, *J. Comput. Phys.*, 215 (2006), 348-362.
- [23] P. Lin, C. Liu and H. Zhang, An energy law preserving C^0 finite element scheme for simulating the kinematic effects in liquid crystal flow dynamics, *J. Comput. Phys.*, 227 (2007), 1411-1427.
- [24] Z. L. Guo, P. Lin and Y. F. Wang, Continuous finite element schemes for a phase field model in two-layer fluid Benard-Marangoni convection computations, *Comput. Phys. Comm.*, 185

- (2014), 63-78.
- [25] K. Bao, Y. Shi, S. Sun and X. P. Wang A finite element method for the numerical solution of the coupled Cahn-Hilliard and Navier-Stokes system for moving contact line problems, *J. Comput. Phys.*, 231 (2012), 8083-8099.
 - [26] P. Spelt, Shear flow past two-dimensional droplets pinned or moving on an adhering channel wall at moderate Reynolds numbers: A numerical study, *J. Fluid Mech.*, 561 (2006), 439-463.
 - [27] A. D. Schleizer and R. T. Bonnecaze, Displacement of a two-dimensional immiscible droplet adhering to a wall in shear and pressure driven flows, *J. Fluid Mech.*, 383 (1999), 29-54.
 - [28] X. F. Yang, J. J. Feng, C. Liu and J. Shen, Numerical simulations of jet pinching-off and drop formation using an energetic variational phase-field method, *J. Comput. Phys.*, 218 (2006), 417-428.
 - [29] P. Lin, C. Liu and H. Zhang, An energy law preserving C^0 finite element scheme for simulating the kinematic effects in liquid crystal dynamics, *J. Comput. Phys.*, 227 (2007), 1411-1427.
 - [30] R. Altmann and J. Heiland, Finite element decomposition and minimal extension for flow equations, Preprint 2013-11, Technische Universität Berlin, Germany, 2013.
 - [31] P. Lin, A sequential regularization method for time-dependent incompressible Navier-Stokes equations, *SIAM J. NUMER. ANAL.*, 34 (1997), 1051-1071.
 - [32] M. Arnold, Half-explicit Runge-Kutta methods with explicit stages for differential-algebraic systems of index 2, *BIT Numer. Math.*, 38 (1998), 415-438.
 - [33] M. Arnold, K. Strehmel and R. Weiner, Half-explicit Runge-Kutta methods with explicit stages for differential-algebraic equations of index 1, *Numer. Math.*, 64 (1993), 409-431.
 - [34] P. Yue, C. Zhou and J. J. Feng, Sharp-interface limit of the Cahn-Hilliard model for moving contact lines, *J. Fluid Mech.*, 645 (2010), 279-294.
 - [35] P. Yue and J. J. Feng, Wall energy relaxation in the Cahn-Hilliard model for moving contact lines, *Phys. Fluids*, 23 (2011), 012106: 1-8.
 - [36] Y. Sui and P. D. M. Spelt, An efficient computational model for macroscale simulations of moving contact lines, *J. Comput. Phys.*, 242 (2013), 37-52.
 - [37] Y. Sui and P. D. M. Spelt, Validation and modification of asymptotic analysis of slow and rapid droplet spreading by numerical simulation, *J. Fluid Mech.*, 715 (2013), 283-313.
 - [38] Y. Sui, H. Ding and P. D. M. Spelt, Numerical Simulations of Flows with Moving Contact Lines, *Annu. Rev. Fluid Mech.*, 46 (2014), 97-119.